Journal of Geophysical Research: Solid Earth

RESEARCH ARTICLE
10.1029/2018JB015548

On the Magnetism Behind the Besnus Transition in Monoclinic Pyrrhotite

Dimitrios Koulialias[1,2], Robin Schäublin[2], Güven Kurtuldu[2], Peter G. Weidler[3], Jörg F. Löffler[2], and Andreas U. Gehring[1]

[1]Institute of Geophysics, Department of Earth Sciences, ETH Zurich, Zurich, Switzerland, [2]Laboratory of Metal Physics and Technology, Department of Materials, ETH Zurich, Zurich, Switzerland, [3]Institute of Functional Interfaces, Karlsruhe Institute of Technology, Karlsruhe, Germany

Key Points:
- The Besnus transition in monoclinic pyrrhotite is indicated by a magnetic anomaly at a temperature of about 30 K
- The magnetic anomaly is due to the interaction of local anisotropy fields stemmed from the ordered arrangement of vacancies in the crystal
- The link between defect structure and magnetism provides a new path to constrain physicochemical conditions during pyrrhotite formation

Correspondence to:
A. U. Gehring,
agehring@ethz.ch

Citation:
Koulialias, D., Schäublin, R., Kurtuldu, G., Weidler, P. G., Löffler, J. F., & Gehring, A. U. (2018). On the magnetism behind the Besnus transition in monoclinic pyrrhotite. *Journal of Geophysical Research: Solid Earth*, *123*. https://doi.org/10.1029/2018JB015548

Received 26 JAN 2018
Accepted 22 JUL 2018
Accepted article online 31 JUL 2018

Abstract In monoclinic 4C pyrrhotite (ideal formula Fe_7S_8), ordered vacancy distribution forms a superstructure with strong ferrimagnetism that makes this mineral a major remanent magnetization carrier in the Earth's crust. The pronounced decrease in isothermal remanence magnetization at about 32 K, known as Besnus transition, is a characteristic trait that marks the low-temperature transition in 4C pyrrhotite, and it is used as a key to identify this mineral phase in rock samples. Here we take a nearly pure single pyrrhotite crystal ($Fe_{6.97}S_8$) from the Swiss Alps to study its Besnus transition in a broad mineral-magnetic approach that combines detailed structural analysis with static and dynamic magnetization experiments. All the magnetic properties inferred from the experimental data are discussed in the context of a recent model that explains interacting anisotropy fields in the 4C pyrrhotite caused by the vacancy arrangement as the origin of the Besnus transition.

1. Introduction

Pyrrhotite refers to a structurally complex iron monosulfide solid solution series across the chemical composition $Fe_{1-x}S$ with $0 \leq x \leq 0.125$. These monosulfides have attracted considerable interest in fundamental magnetism over decades because the variation in the magnetic properties is critically affected by the iron deficiency (Armstrong et al., 2013; Herbert et al., 2015; Néel, 1953; Pauthenet, 1952; Pearce et al., 2006; Schwarz & Vaughan, 1972; Weiss, 1899). Pyrrhotite phases have a distorted NiAs-type structure in common where the iron atoms occupy the interstitials in a hexagonal close-packed array of sulfur. Unoccupied octahedral Fe sites generate variable stacking sequences of vacancy and full sublattices that result in different superstructures. In the monoclinic end-member Fe_7S_8 with the highest iron deficit, the alternation of full and ordered vacancy sublattices yields a superstructure with four times periodicity along the *c*-axis compared to the NiAs-type substructure and is therefore denoted 4C pyrrhotite (Bertaut, 1953). In this commensurate superstructure, the Fe magnetic spins have ferromagnetic order within the *c*-plane and antiferromagnetic coupling between adjacent sublattices along the *c*-axis, and this configuration accounts for a strong ferrimagnetism (e.g., Néel, 1953). This ferrimagnetism in combination with its widespread occurrence makes the 4C pyrrhotite a major natural remanence carrier in the Earth's crust and in extraterrestrial materials (e.g., Kontny et al., 2000; Rochette et al., 1990; Rochette et al., 2001). Magnetic information obtained from 4C pyrrhotite has been successfully applied in a wide range of rock and paleomagnetic studies, which include the reconstruction of orogens and diagenetic processes (Appel et al., 2012; Friedman et al., 2014; Gillett, 2003; Honsho et al., 2016; Kars et al., 2015; Manning & Elmore, 2012; Schill et al., 2003; Weaver et al., 2002; Wright, 1966), or the inference of the magnetic effects of shock metamorphism in impact structures on Earth and Mars meteorites (Louzada et al., 2007; Mang et al., 2012; Rochette et al., 2001).

Key to the magnetic identification of 4C pyrrhotite in geological samples is its characteristic low-temperature magnetic transition at $T \approx 30$ K, also known in the rock magnetic community as the Besnus transition (Rochette et al., 2011). This transition is defined not only by pronounced decrease in remanence magnetization upon cooling but also in other physical properties such as resistivity (e.g., Besnus & Meyer, 1964; Charilaou et al., 2015). Despite the fact that the low-temperature transition has been successfully used to identify 4C pyrrhotite in rock materials, the physics behind this phenomenon is still a matter of debate. The main controversy is whether the transition is of crystallographic or magnetic origin (e.g., Charilaou et al., 2015; Fillion & Rochette, 1988; Kind et al., 2013; Volk et al., 2016; Wolfers et al., 2011). A reason for the lack of a

generally accepted model is probably the richness of physical features associated with the transition. Wolfers et al. (2011) interpreted a set of neutron diffraction data of and the appearance of a fourfold magnetic rotational symmetry in a natural pyrrhotite with pronounced twinning in favor of a crystallographic change from monoclinic to triclinic associated with the transition. A detailed neutron diffraction study on synthetic 4C pyrrhotite powder samples, however, revealed no indication of a crystallographic change at low temperature (Powell et al., 2004). Moreover, a recent experimental and numerical study of a natural pyrrhotite crystal provided compelling evidence that the emergent fourfold rotational symmetry at $T < 30$ K is due to interacting local anisotropy fields in 4C pyrrhotite (Koulialias, Charilaou, Schäublin, et al., 2018). These fields stem from two groups of Fe sites in 4C pyrrhotite, which differ in their geometrical relation to the vacancies. One group contains the Fe sites with interlayer vacancies as next neighbors, and the other group the remaining Fe sites. The spatial arrangement of the groups forms a 30° angle (Koulialias, Charilaou, Schäublin, et al., 2018; Koulialias, Charilaou, Mensing, et al., 2018). Furthermore, the different local anisotropy properties in 4C pyrrhotite that were first postulated by Adachi (1963) based on theoretical considerations can lead to an incoherent out-of-plane spin rotation. Magnetic torque analysis by Koulialias, Charilaou, Mensing, et al. (2018) experimentally confirmed the incoherent spin rotations and further showed that reversed spin rotation occurs at about $T \approx 30$ K. This finding provides further evidence for the critical interaction of the different local anisotropy fields associated with the Besnus transition. The interaction model is similar to that by Charilaou et al. (2015) but localizes interacting anisotropy fields in the 4C superstructure and not between polymorphous superstructures. The new view to the low-temperature transition, however, challenges the prevalent idea that the Besnus transition is caused by a crystallographic change that lowers the symmetry as it is known for the classic Verwey transition in magnetite. Here we present detailed static and dynamic magnetization data as well as structural data of a nearly pure 4C pyrrhotite in order to discuss the low-temperature transition in the light of the new interaction model and its consequence for the debate of the Besnus transition in the rock magnetic community.

2. Materials and Methods

A pyrrhotite crystal from a headrace gallery in the Aar Massif near Amsteg in Canton Uri, Switzerland, was used. In this Massif, which includes a large gneiss complex and a metasediment cover formed during Alpine orogeny, various tunnel projects over the last few decades have shown that apart from pyrite, pyrrhotite is the most abundant iron sulfide in this rock body (Amacher & Schüpbach, 2011). The mineralogy of pyrrhotite crystals from the same locality near Amsteg has been reported in the literature and exhibits a complex crystallographic structure that may originate from the intergrowth of different phases (Engel et al., 1978).

The structural and magnetic analyses of the pyrrhotite crystal generally follow the methodological strategy previously reported by Koulialias et al. (2016). This permits an optimal comparison between different pyrrhotite samples. The crystallographic properties of our pyrrhotite were measured by powder X-ray diffractometry (XRD) with Cu $K_{\alpha 1,2}$ radiation in θ-θ geometry on a Bruker D8 Advance instrument, equipped with a position-sensitive detector Lynxeye®, from 14 to 93°2θ with a step width of 0.011°2θ and a total counting time per step of 168 s. The powder was placed in the 0.5-m-deep indention (diameter 20 mm) of the sample holder and gently smoothed. Rietveld refinement was performed with the Bruker software TOPAS (Bruker AXS TOPAS V4.2, 2008) using the fundamental parameter approach (Cheary & Coelho, 1992). The structure model for 4C pyrrhotite was taken from Tokonami et al. (1972), and, besides the lattice parameters, the occupancies of the Fe positions in the structure were refined. The structure model of quartz was obtained from the Crystallography Open Database (Grazulis et al., 2009).

To complement the structural bulk analysis, differential scanning calorimetry (DSC) on a 10.9-mg crystal flake was performed with a heating rate of 20 K/min using a Mettler-Toledo DSCI/700 device. Transmission electron microscopy (TEM) was conducted on an FEI Talos equipped with a field-emission gun and operated at 200 kV. Imaging was performed in TEM bright-field. Selected area diffraction patterns were obtained to identify the crystallographic phase of the sample and to derive the relative orientations of the observed areas. The diffraction patterns were analyzed with jEMS software (Stadelmann, 1987). Diffraction patterns of the various crystallographic pyrrhotite models reported in literature were employed in order to obtain the best match between experimental and simulated data.

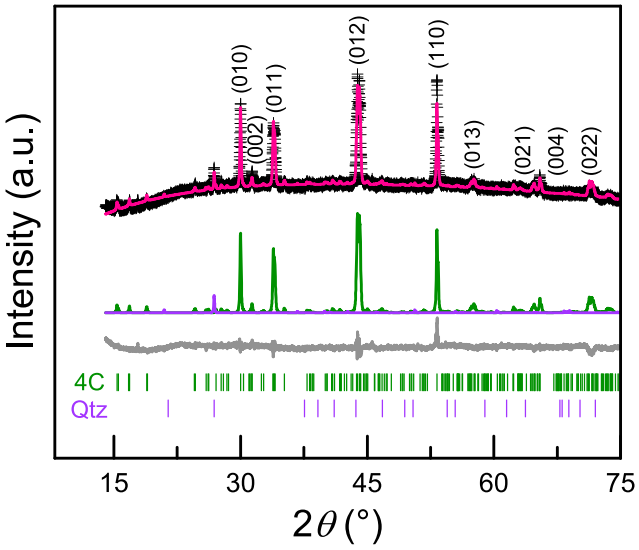

Figure 1. Powder X-ray diffractogram of the pyrrhotite sample with measured data (crosses) and calculated pattern (red line) as the sum of the refined 4C pyrrhotite (green) and quartz pattern (blue). The gray line at the bottom is the difference of the measured and calculated patterns. The peaks of the NiAs-type substructure are indexed in the calculated pattern.

The cation content of the pyrrhotite crystal was determined by wet chemical analysis with inductively coupled plasma optical emission spectrometery after microwave digestion in HNO_3/H_2O_2. The thermal stability and the magnetic ordering temperature were measured by high-temperature magnetic susceptibility on a powder sample under argon atmosphere with a KLY-3 Kappabridge coupled to a thermoelement. The heating/cooling rate was about 10 K/min. The dynamic and static magnetization experiments on a crystal oriented in the *c*-plane of the NiAs-like substructure were performed between 300 and 10 K using a Physical Property Measurement System (Quantum Design). The hysteresis parameters at different temperatures were recorded after zero-field cooling (ZFC) the sample from room temperature, carrying an isothermal remanence magnetization (IRM) acquired in a 3-T field. The remanent coercivity (B_{cr}) was determined from the hysteresis loop using the method by Jackson et al. (1990). In addition, the hysteresis curve at 10 K was measured after field cooling (FC) in a 3-T field. The cooling/warming curves of the IRM acquired at room temperature were recorded in a 2-mT field in order to compensate the weak magnetometer-immanent, residual magnetic field in the coil. The heating behavior of the IRM acquired at 10 K was examined after ZFC and FC in a 3-T field. Moreover, the same sample was taken to measure the first-order reversal curves at room temperature on a MicroMag 3900 vibrating-sample magnetometer with a step size of 1.2 mT and a maximum field of 1 T. The plots were made by using the MATLAB code FORCOBELLO with a smoothing factor 4 (Winklhofer & Zimanyi, 2006).

3. Results and Discussion

3.1. Chemical and Structural Properties

In the X-ray diffractogram all reflections can be assigned to a pyrrhotite phase and traces of quartz (Figure 1). The major peaks are caused by the hexagonal NiAs-type substructure of the pyrrhotite, with $a = b = 3.4379$ nm and $c = 5.7001$ nm and $c/a = 1.658$. This ratio suggests that the bonds in the hexagonal close-packed structure are mainly covalent with weak ionic character (e.g., Sakkopoulos et al., 1986). The expected 4C superstructure was best described by Rietveld refinement using the structural model based on the space group *F*2/*d* as proposed by Tokonami et al. (1972). The obtained unit cell parameters were $a = 1.19126 \pm 0.005$ nm, $b = 0.6819 \pm 0.0003$ nm, $c = 2.2798 \pm 0.0008$ nm, and $\beta = 90.508 \pm 0.002°$, with a goodness of fit of 1.82, a weighted Durbin Watson value of $d = 0.62$, and a R-Bragg factor of 1.75. Moreover, the refinement of the Fe occupancy factor yielded a calculated nearly stoichiometric chemical composition of $Fe_{6.97}S_8$ for the 4C pyrrhotite. The chemical analysis of the pyrrhotite crystal shows an Fe concentration of 59.3 ± 0.7 wt%, which is slightly lower than the calculated 60.1 wt% obtained from XRD. The difference can, to some extent, be explained by the concentration of minor cations of about 0.1 wt%, which includes 650-ppm Ni and 750-ppm Mn.

The TEM micrographs revealed a variety of crystal defects that sectioned the 4C pyrrhotite (Figure 2a). Selected area electron diffraction only exhibited patterns of 4C pyrrhotite that could be simulated using the crystallographic model of Tokonami et al. (1972), which considers the space group *F*2/*d* with $a = 1.1902 \pm 0.0008$ nm, $b = 0.6859 \pm 0.0005$ nm, $c = 2.2787 \pm 0.0001$ nm, and $\beta = 90.43°$ for a 4C pyrrhotite single crystal (Figures 2a and 2b).

Two different systems of planar defects can be distinguished, which consist of either parallel or nonparallel lamellae with respect to the *c*-plane of the hexagonal substructure (Figures 2a and 2b). The parallel lamellae are in the micrometer size range, and selected area diffraction patterns show that these lamellae are rotated to each other in the *c*-plane by a 60° angle (Figure 2a). Such twins are often observed in monoclinic pyrrhotite (e.g., Harries et al., 2011; Keller-Besrest et al., 1982; Pósfai et al., 2000; Pierce & Buseck, 1974; Van Landuyt & Amelinckx, 1972), and they were most likely formed during the crystal growth.

The lamellae with nonparallel contrasts with respect to the *c*-plane are characteristic of stacking faults marked by jogs due to dislocation cross-slip, which indicate shearing by mechanical stress (Figures 2a and

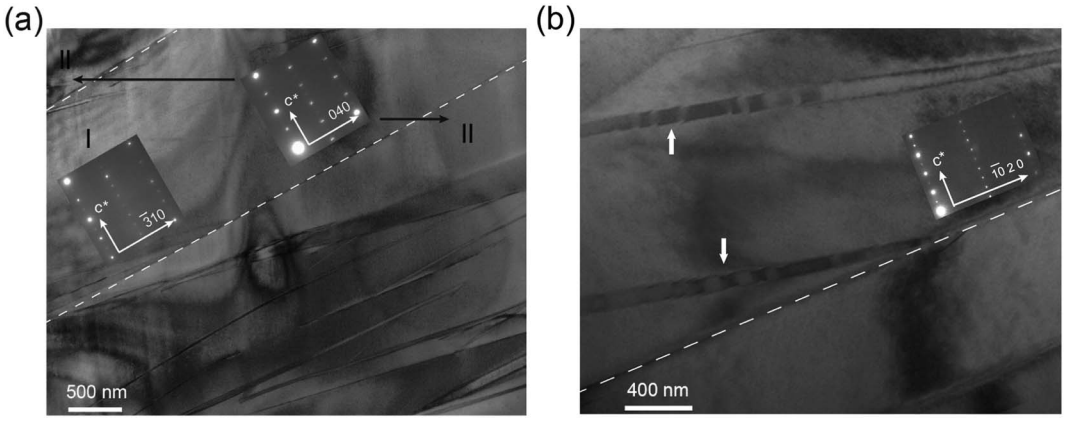

Figure 2. Transmission electron micrographs show twins with 60° rotation at the twin boundaries in the *c*-planes (dashed lines) inferred from the diffraction patterns (insets) of (a) lamellae I and II (arrowed) with zone axes [130] and [100], respectively, of the 4C pyrrhotite structure and (b) stacking faults forming jogs (arrowed) and intersections with the *c*-plane.

2b). Such features accord with the observation that pyrrhotite generally undergoes plastic deformation in orogenic processes (e.g., Clark & Kelly, 1973; Graf & Skinner, 1970). It was experimentally shown that pyrrhotite single crystals exhibit a low resistance of the lattice to shear in the *c*-plane, but the angle of the load critically affects the slip plane and direction, which can thus be out of the *c*-plane (Kübler, 1985). The mechanically induced defects suggest that both the hexagonal substructure and the superstructure critically affect the deformation architecture in our single crystal. From this it follows that the load on the crystal over a geological period of time locally broke the stacking modulation, and this in turn created areas in the 4C pyrrhotite with perturbed cation ordering of the crystal. Given this, the studied crystal can be described as a twinned 4C pyrrhotite single crystal mechanically deformed during Alpine orogeny.

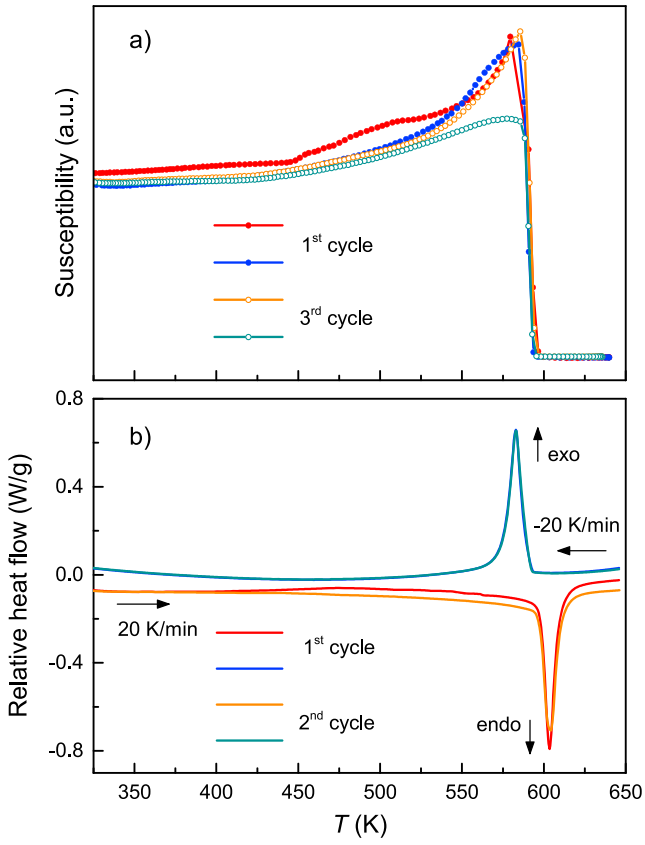

Figure 3. (a) High-temperature susceptibility cycles of the powdered pyrrhotite crystal with heating (red dots) and cooling (blue dots) curves of the untreated sample and after two heating-cooling cycles (orange and green circles); (b) two differential scanning calorimetry cycles with heating curves (red and orange) and cooling curves (blue and green), where the latter lie exactly on top of each other.

3.2. Magnetic Properties of the Pyrrhotite Crystal

3.2.1. High-Temperature Susceptibility and Calorimetry

The susceptibility-versus-temperature curves show a Curie temperature T_c = 596.6 ± 0.2 K (Figure 3a). Such T_c is typical of ferrimagnetic 4C pyrrhotite (Li & Franzen, 1996; Powell et al., 2004). The initial heating curve exhibits a kink at about 450 K and a peak prior to T_c that can be explained by the Hopkinson effect (Dunlop & Özdemir, 1997). A magnetic change in pyrrhotite at $T \approx 450$ K is well known and has been explained by an antiferromagnetic-to-ferrimagnetic λ transition due to vacancy rearrangement mainly associated with a 5C superstructure (Herbert et al., 2015; Kontny et al., 2000; Marusak & Mulay, 1980). Upon cooling, the kink vanishes, accompanied by no significant change in the bulk susceptibility at room temperature (Figure 3a). The absence of a significant increase in susceptibility in the heated sample argues against the formation of a ferrimagnetic phase at the expense of an antiferromagnetic one. The two cycles of the DSC analysis show in the heating curves endothermic peaks at T = 604 K and an enthalpy change ΔH = 16.6 J/g (Figure 3b). The cooling curves are identical for both cycles and exhibit an exothermic peak at T = 582 K and ΔH = 20.4 J/g. The onsets of the endothermic and exothermic peaks occur at 595.1 ± 2.8 K, i.e., the temperature where the T_c is found in the susceptibility measurements (Figures 3a and 3b). This similarity confirms that the ferrimagnetic-to-paramagnetic transition takes place simultaneously with the change from the 4C to 1C structure due to the randomization of the vacancy order

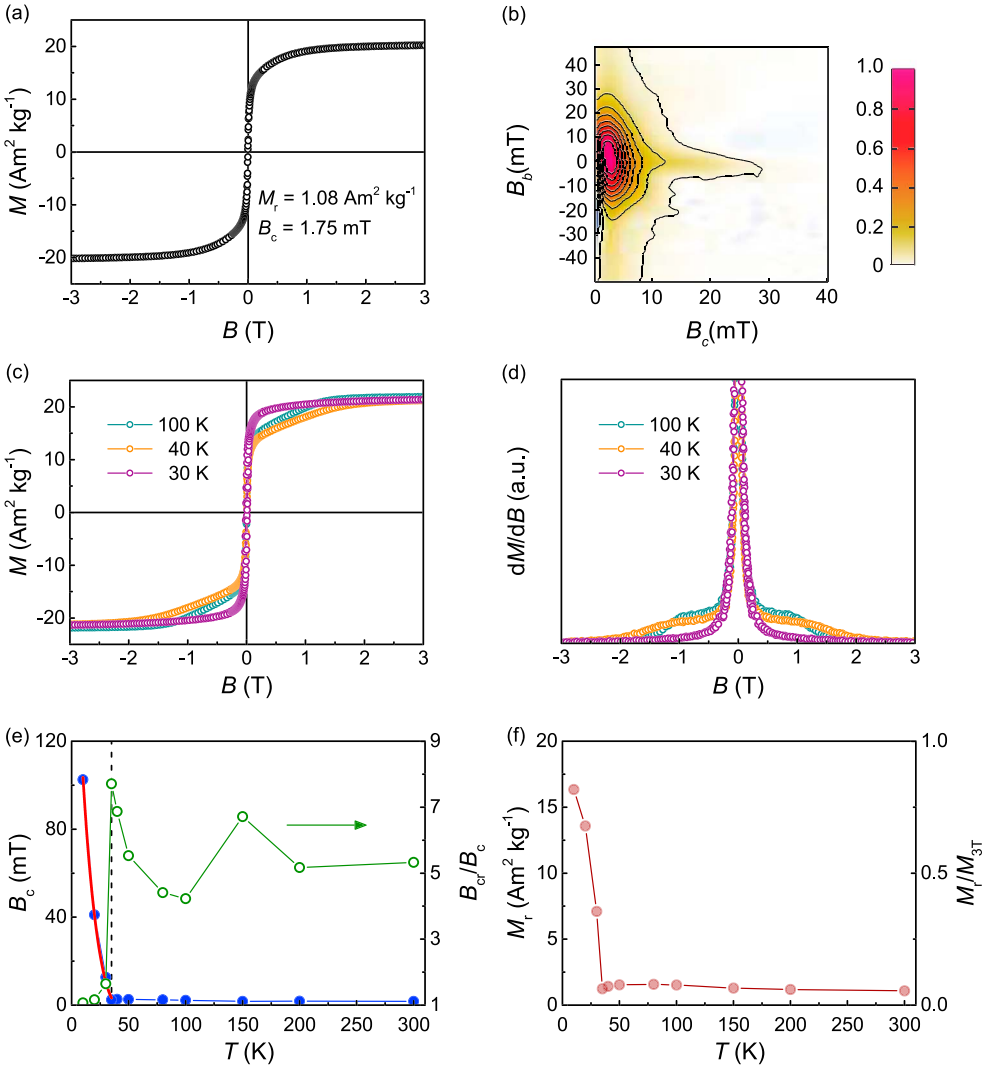

Figure 4. (a) $M(B)$ curve measured in the c-plane at room temperature and (b) the corresponding first-order reversal curve diagram with smoothing factor 4, (c) $M(B)$ curves at low temperature and (d) the dM/dB of the hysteresis curves; (e) temperature dependence of B_c with the fitting after Gaunt (1983) at $T < 35$ K (red line) and the coercivity ratio. The dashed vertical line highlights the Besnus transition; and (f) temperature dependence of remanence and squareness ratio.

(e.g., Powell et al., 2004). With this in mind, the difference in the peak positions between heating and cooling is then most likely a cation diffusion effect. Moreover, the comparison of the two heating curves shows a slightly different behavior with a bifurcation at $T \approx 425$ K. This weak enthalpy change is close to the temperature where the kink in the first heating curve of the susceptibility cycle occurs. Given this, it can be assumed that the thermally induced changes stem from irreversible cation rearrangements on a relatively small scale in the 4C pyrrhotite. Considering the TEM micrographs, this rearrangement is likely associated with mechanically deformed zones.

3.2.2. Static Magnetic Properties

Monoclinic 4C pyrrhotite has a strong magnetic anisotropy with easy axes in the c-plane and a striking hard one along the c-axis of the hexagonal NiAs-type substructure (Weiss, 1907). In this study, we performed only magnetic measurements parallel to the c-plane of the crystal. The hysteresis curve at room temperature (Figure 4a) shows a coercivity $B_c = 1.75$ mT, a near saturation magnetization at 3 T (M_{3T}) of 20.19 Am^2/kg (e.g., Néel, 1953), a remanence magnetization $M_r = 1.08$ Am^2/kg, and a squareness ratio $M_r/M_{3T} = 0.05$. The remanent coercivity B_{cr} deduced from the hysteresis loop is 9.3 mT, which leads to a coercivity ratio of $B_{cr}/B_c = 5.3$. The coercivity ratio and M_r/M_{3T} are typical of 4C pyrrhotite in a multidomain state, generally

with 180° domain walls (Ds) normal to the *c*-axis of the pyrrhotite crystal (Halgedahl & Fuller, 1981; O'Reilly et al., 2000). The M_{3T} is close to magnetization at saturation estimated for stoichiometric Fe_7S_8 pyrrhotite (Néel, 1953) and measured in natural samples (Armstrong et al., 2013; Halgedahl & Fuller, 1981), but it is clearly higher than in a pyrrhotite crystal that contains epitaxially intergrown poly-type, monoclinic superstructures (Koulialias et al., 2016). For our pyrrhotite crystal a magnetic moment per formula unit $Fe_{6.97}S_8$ of 2.34 μ_B was calculated. This value is significantly higher than the 2.03 μ_B found by Bertaut (1953), which relies on an ionic model with a 4C pyrrhotite formula of $Fe_2^{3+}Fe_5^{2+}S_8^{2-}$. Mössbauer spectroscopy, however, provides no evidence for the presence of Fe^{3+} cations in 4C pyrrhotite, and the $c/a = 1.658$ obtained from XRD suggests covalent bonding with a weak ionic character (e.g., Fillion et al., 1992; Hafner & Kalvius, 1966; Oddou et al., 1992; Sakkopoulos et al., 1986). In a recent X-ray magnetic circular dichroism study, Letard et al. (2007) confirmed the exclusive Fe^{2+} valence state in natural pyrrhotite and showed that the cations comprise, apart from the spin moment, a contribution from the orbital moment of about 15%, and this in turn can explain the 2.34 μ_B calculated for our sample.

As mentioned above, the hysteresis properties of the pyrrhotite are typical of multidomain single crystals. The first-order reversal curve analysis provides evidence of a broader range of B_c (Figure 4b). Apart from the largest contribution with $B_c < 5$ mT, a coercivity spectrum that forms a faint ridge up to 25 mT is visible. Because the pyrrhotite sample is a single crystal, grain- size effects described by Dekkers et al. (1989) as a cause of the coercivity range can be excluded. With this in mind the microcoercivity population may originate from dislocations due to crystal deformation (Lindquist et al., 2015).

Low-temperature measurements exhibit minor changes in the hysteresis parameters M_r and B_c down to 35 K (Figures 4c–4f). The coercivity ratio B_{cr}/B_c, however, shows a local minimum at 100 K and a pronounced increase down to 35 K. Moreover, between 150 and 40 K, $M(B)$ behaves nonuniformly upon approaching saturation, as indicated by the shoulder in dM/dB (Figures 4c and 4d). The shoulder is symmetrical with respect to the ascending and descending branches of the hysteresis loop and shifts to higher fields, with 1 T at 100 K and 1.3 T at 40 K (Figure 4d). A similar noncollective way to reach saturation as indicated by peaks in dM/dB was reported in the literature (Koulialias et al., 2016; Volk et al., 2016). Based on XRD and magnetic data, Koulialias et al. (2016) attributed this behavior to two different anisotropy systems stemmed from a 4C and an additional polymorph superstructure termed as 5C*. A recent experimental and numerical study that combined TEM and magnetic torque data revealed two different local anisotropy systems in the 4C pyrrhotite, and this in turn suggests that no additional superstructure is needed to generate an inflection point (Koulialias, Charilaou, Schäublin, et al., 2018). The two local anisotropy systems caused by two groups of Fe sites, which differ in their positions to the vacancy sites, are further indicated by the incoherent out-of-plane spin rotation at $T < 200$ K (Koulialias, Charilaou, Mensing, et al., 2018). Volk et al. (2016) proposed that the inflection point, which also showed an angular dependence, is due to easy-axes switching in the *c*-plane somewhat analogous to an isotropic point where the magnetocrystalline anisotropy constants change their signs. No indication for such change, however, was found in the magnetic torque measurements by Koulialias, Charilaou, Schäublin, et al. (2018). Moreover, the occurrence of inflection points in the hysteresis loops in a wide temperature range 35 to 20 K also argues against easy-axes switching and is in favor of a heterogeneous anisotropy system.

At 30 K, $M(B)$ increases coherently (Figures 4c and 4d). Considering the findings by Koulialias, Charilaou, Schäublin, et al. (2018) and Koulialias, Charilaou, Mensing, et al. (2018), this behavior can be explained by the interaction of the local anisotropy fields in the 4C pyrrhotite. This interaction is temperature dependent and results in progressive magnetic hardening as indicated by the increase in B_c and M_r upon cooling (Figures 4e and 4f). It is worth noting that the B_c behavior associated with the Besnus transition is different from that of a single-crystal magnetite at the Verwey transition where a sharp increase in B_c points to a crystallographic change (Özdemir, 2000). Continuous hardening, however, was reported for other 4C pyrrhotite samples and was interpreted by annihilation of domains in the bulk material (e.g., Dekkers et al., 1989) or by strong pinning that impedes DW motions (Kind et al., 2013). In our crystal, B_c at $T \leq 35$ K can be fitted by ${B_c}^{1/2} \propto T^{2/3}$ with a quality factor $R^2 = 0.994$ (Figure 4e). Based on theoretical considerations, such relation can be attributed to thermally activated unpinning (Gaunt, 1983). Here, it is worth noting that the law of B_c increase in a pyrrhotite powder sample is different (Kind et al., 2013).

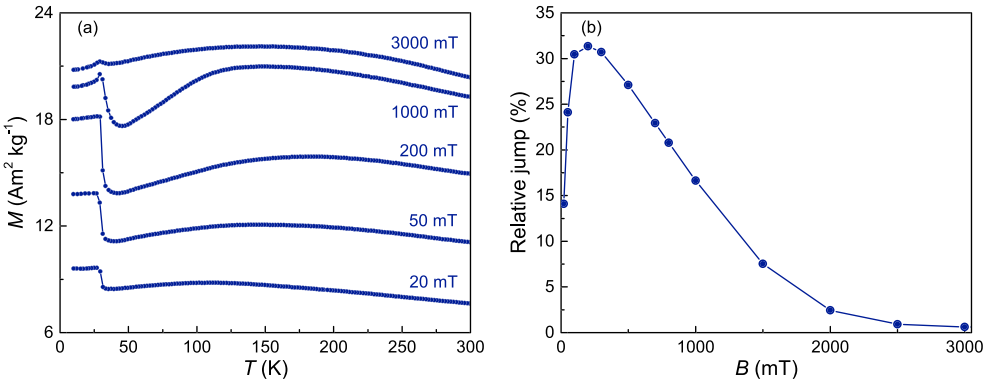

Figure 5. (a) FC magnetizations in the *c*-plane; (b) relative increase in the FC magnetization between 40 and 20 K as a function of the applied magnetic field.

The low-temperature transition is also manifested by a field-dependent magnetization jump in the temperature range between 40 and 20 K (Figures 5a and 5b). The relative increase in magnetization reaches a maximum in a $B = 200$ mT field of about 30% and drops to 3% in a $B > 2{,}000$ mT field (Figure 5b). The course of the FC curves, however, points to a competition between the potential magnetization energy (Zeeman energy E_z) and the anisotropy (E_{an}) energy (Koulialias, Charilaou, Schäublin, et al., 2018). The global or local minimum in the FC curves at $T \approx 35$ K marks a maximum in E_{an}, and the subsequent relative jump points to a pronounced decrease in E_{an}. Considering the closure of the hysteresis loops, DW motions critically affect the jumps at $B < 300$ mT. Moreover, the pronounced decrease in E_{an} occurs in the same temperature range as the disappearance of the shoulders in dM/dB (Figures 4c and 4d). Because the shoulder most likely originates from the superposition of two anisotropy systems, its disappearance can be explained by their interaction. Koulialias, Charilaou, Schäublin, et al. (2018) showed that such interaction generates an additional mixed energy term that acts against E_{an} and results in the emergence of a fourfold magnetic rotational symmetry found in 4C pyrrhotite at $T < 40$ K (Volk et al., 2016; Wolfers et al., 2011).

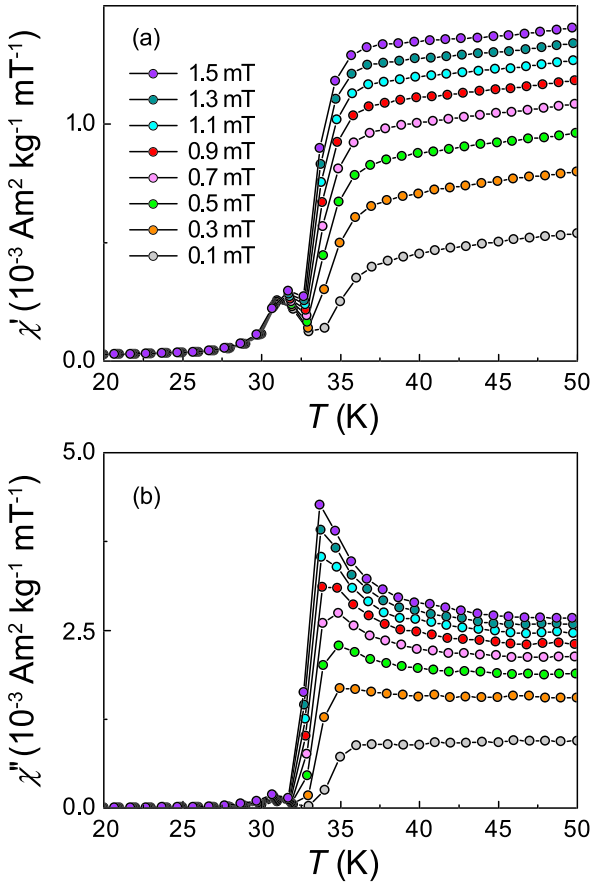

Figure 6. Amplitude dependence of the ac susceptibility in the *c*-plane of the NiAs-type substructure as a function of temperature with (a) in-phase susceptibility χ' and (b) out-of-phase susceptibility χ''.

3.2.3. Dynamic Magnetic Properties

An insight into the magnetic dynamics of the low-temperature transition is provided by magnetic *AC* susceptibility measurements (Figure 6). Over the entire low-temperature range no frequency dependence was found. Both the in-phase χ' and the out-of-phase χ'', however, exhibit an amplitude dependence between 300 and 32 K, which most likely originates from DW motion (Kind et al., 2013). Below 35 K, χ' drops and forms a local minimum at 33 K followed by a weak peak and a flattening at $T < 30$ K. With the drop, the amplitude dependence declines and disappears at 30 K, and this indicates an increase in the DW energy. The out-of-phase susceptibility χ'' with 0.1-mT amplitude reveals a similar decrease as observed for χ'. With increasing amplitude, however, a peak in χ'' evolves and is well developed in $B = 1.5$ mT at $T = 34$ K. The field-dependent gain in dissipation indicates irreversible DW motions that start at $T \approx 35$ K. The cessation of dissipative processes below 34 K suggests then an enhancement in the total interaction energy between the DWs and lattice defects, leading to a pinning regime which causes significant hardening as documented in the continuous increase in B_c at $T < 35$ K (Figures 4e and 4f).

3.2.4. Magnetic Remanence

Additional information about the demagnetization associated with the change of the pinning regime is obtained from the temperature dependence of M_r acquired in a 3-T field at 300 and 10 K, referred to as

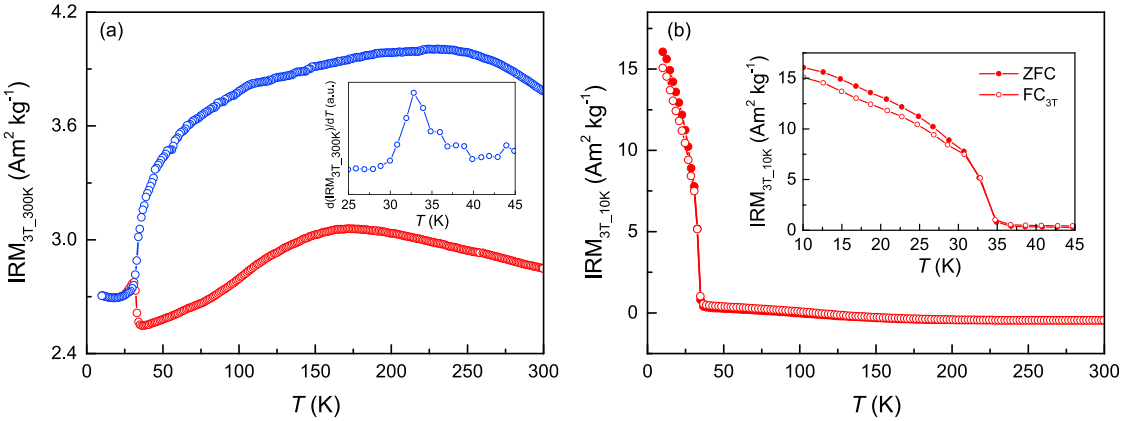

Figure 7. (a) Cooling (blue circles) and heating (red circles) cycle of isothermal remanent magnetization acquired in a 3-T field at 300 K and recorded in a 2-mT field, with the first derivative of the cooling curve between 25 and 45 K as inset; (b) heating curve of isothermal remanence acquired at 10 K in a 3-T field after zero-field cooling (ZFC) of the sample (red dots) and after field cooling (FC) of the sample in a 3-T field (red circles), with the two steps of remanence decay up to 35 K shown in the inset. The slightly negative values of IRM_{3T_10K} are induced by the residual field in the coil.

isothermal remanent magnetization IRM_{3T_300K} and IRM_{3T_10K}, respectively (Figure 7). Upon cooling, the IRM_{3T_300K} begins to decrease at about 200 K with a distinct drop between 40 and 30 K, followed by a nearly constant behavior (Figure 7a). The loss of remanence is most likely due to changes in E_{an} that cause irreversible rotations of magnetic moments in the domains. The enhanced decrease in IRM_{3T_300K}, with a maximum slope at T = 34 K that simultaneously occurs with a maximum dissipation (Figures 6b and 7a), suggests a new anisotropy regime. Such a regime was explained by an emergent mixed energy term caused by interacting local anisotropy fields in the 4C pyrrhotite (Koulialias, Charilaou, Schäublin, et al., 2018). This interpretation is in line with the disappearance of the shoulders in dM/dB at $T < 40$ K and the generation of strongly pinned DWs. In the temperature range ($T \leq 30$ K) with interacting local anisotropy fields the cooling and heating IRM_{3T_300K} curves are congruent (Figure 7a). With this in mind the bifurcation upon warming marks the cessation of the local anisotropy field interactions, and this in turn triggers again changes in the domain configuration.

The IRM_{3T} acquisition at 10 K after ZFC induces a new domain configuration in the crystal. The relatively high ratio of 0.8 between ZFC IRM_{3T_10K} and M_{3T} suggests that only a few of the DWs are pinned in the bulk material and the majority is at the surface (Figure 7b). The ZFC IRM_{3T} is about 10% higher compared to the remanent magnetization acquired at 10 K after FC in a 3-T field. Such behavior was described for other multidomain magnetic phases and explained for magnetite and titanomagnetite by changes in the pinning regime due to interactions between crystallographic twins and magnetic domains (Carter-Stiglitz et al., 2006; Church et al., 2011; Kasama et al., 2010). Apart from twins, our crystal contains numerous nonparallel lamellae caused by mechanical deformation, which can lead to additional pinning sites (Figure 2). The lower remanence in the FC case, where the initial condition for the remanence acquisition is a quasi-single domain state, could therefore be a field-induced effect that promotes pinning at mechanical defects. This interpretation accords with the observation that in powder samples of multidomain pyrrhotite with less mechanical defects, the decay of the IRM acquired at 10 K under ZFC and FC conditions has a congruent behavior (Kind et al., 2013). In our pyrrhotite sample, the magnetic hysteresis parameters B_c and M_r/M_{2T} are nearly identical for the ZFC and FC cases and, as in the IRM experiment, the M_r value is also higher in the ZFC case (Figure 8). The striking decrease of ZFC IRM_{3T_10K} and FC-acquired remanence upon warming to 35 K is indicative of DW motions into the pyrrhotite crystal. The loss in remanence upon heating exhibits

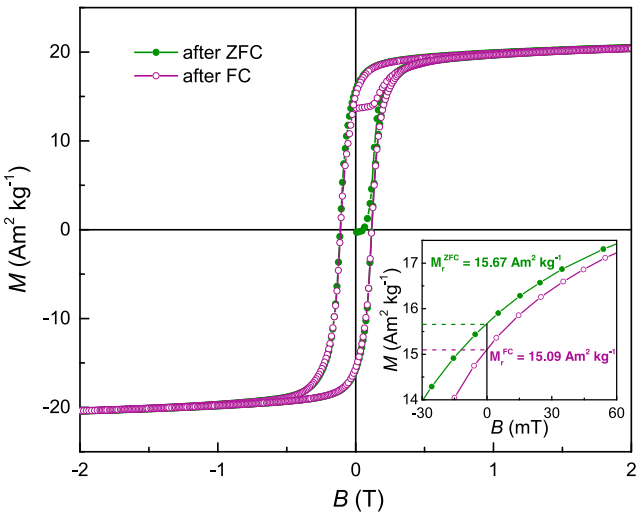

Figure 8. Hysteresis curves recorded at 10 Kup to a 2 T field after zero-field cooling (ZFC; green dots) and after field cooling (FC; purple circles), revealing with slightly different remanent magnetizations (inset).

two steps, a relatively flat decrease up to 32 K followed by a drop to 35 K (Figure 7b). In the flat part the converging decay of the remanences after ZFC and FC points to slight variations of the induced pinning regimes, probably due to mechanical defects. The congruent drop between 32 and 35 K of the ZFC and FC curves marks then the formation of a pinning regime that is generally unaffected by the mechanical crystal defects.

4. Conclusions

In 4C pyrrhotite the defective Fe sites form a superstructure with alternating stacking of full and vacancy sublattices that yields complex magnetic properties with a characteristic low-temperature transition. Our single crystal from the Swiss Alps with a composition of $Fe_{6.97}S_8$ has a crystallographic structure that can be perfectly described in the space group *F*2/*d*. In TEM the crystal exhibits substantial twinning and micro-sized mechanical defects that perturb the overall stacking modulation in the 4C pyrrhotite. The analyses of the static and dynamic magnetizations and the remanence properties in the *c*-plane of the pyrrhotite crystal demonstrate that this micro-sized mechanical perturbation has no critical effect on the Besnus transition at $T \approx 32$ K. The magnetization data show that the hardening of the 4C pyrrhotite below the transition is continuous and occurs simultaneously with the disappearance of the shoulder in d*M*/d*B* detected in the hysteresis loops between about 100 and 35 K. The discontinuity of d*M*/d*B* found over such a wide temperature range is difficult to explain by easy axis switching associated with a crystallographic change at the Besnus transition, as it is generally postulated in the rock magnetic literature (Volk et al., 2016; Wolfers et al., 2011). The model by Koulialias, Charilaou, Schäublin, et al. (2018) and Koulialias, Charilaou, Mensing, et al. (2018) offers an alternative interpretation that accords with the magnetic behavior of 4C pyrrhotite at low temperature. This model explains the transition by the interaction of different local magnetic anisotropy fields in the 4C pyrrhotite that stem from the arrangement of the Fe atoms and their spatial relation to the vacancy sites. Changes in the magnetic interaction pattern at $T \approx 32$ K could theoretically be caused by changes in the Fe-Fe electron-orbital overlap and/or by superexchange interactions (Goodenough, 1963; Lyubutin et al., 2011; Sakkopoulos et al., 1986). The link of the electron-orbital geometry and the change in static magnetization properties proposed by Koulialias, Charilaou, Schäublin, et al. (2018) and Koulialias, Charilaou, Mensing, et al. (2018) agree well with the electronic properties reported for the Besnus transition (e.g., Besnus & Meyer, 1964; Charilaou et al., 2015). The magnetic anisotropy field interaction is also manifested in the dynamic magnetization, which indicates a new pinning regime of the DWs associated with the transition. Given the above, the magnetic response of the Besnus transition mirrors a nontrivial system of Fe sites with different local anisotropy fields in a highly ordered defective crystallographic structure. With this in mind the physical processes behind the Besnus transition are different to those of the Verwey and Morin transitions, which are the two other important transitions in rock and mineral magnetism. The novel interpretation of the magnetic response of the Besnus transition does not hinder its use as a diagnostic feature to detect 4C pyrrhotite in rock bodies. In fact, the effect of the Fe structural arrangement on the magnetic properties may be used to open a new path to further constrain processes of the pyrrhotite formation in geological and extraterrestrial systems.

Acknowledgments
The authors are grateful to Jessica Kind and Michalis Charilaou for the critical discussion of the paper, and to the support of the Scientific Centre for Optical and Electron Microscopy (ScopeM) at ETH Zurich. The project was financed by the Swiss National Science Foundation, Grant 200021-153173. The pyrrhotite material from Uri (Switzerland) is deposited in the mineral collection at ETH Zurich, and all the experimental data are presented in the text and the eight figures.

References

Adachi, K. (1963). Origine de l'énergie d'anisotropie magnétocristalline de la pyrrhotine. *Journal de Physique*, *24*(10), 725–731. https://doi.org/10.1051/jphys:019630024010072500

Amacher, P., & Schüpbach, T. (2011). NEAT-Mineralien: Kristall-Schätze tief im Berg, Amsteg: Geo-Uri, ISBN: 978-3-033-03111-1.

Appel, E., Crouzet, C., & Schill, E. (2012). Pyrrhotite remagnetizations in the Himalaya: A review. In R. D. Elmore, et al. (Eds.), *Remagnetization and Chemical Alteration of Sedimentary Rocks, Geological Society London Special Publications* (Vol. 371, pp. 163–180).

Armstrong, J. N., Hua, S. Z., & Chopra, H. D. (2013). Anisotropic Curie temperature materials. *Physica Status Solidi B: Basic Solid State Physics*, *250*(2), 387–395. https://doi.org/10.1002/pssb.201248186

Bertaut, E. F. (1953). Contribution à l'étude des structures lacunaires: la pyrrhotine. *Acta Cryst*, *6*(6), 557–561. https://doi.org/10.1107/S0365110X53001502

Besnus, M. J., & Meyer, A. J. (1964). Nouvelles données expérimentales sur le magnétisme de la pyrrhotine naturelle. *Proceedings of the International Coneference on Magnetism*. Nottingham, 20, 507–511.

Bruker AXS TOPAS V4.2 (2008). *General Profile and Structure Analysis Software for Powder Diffraction Data. User's Manual*. Karlsruhe, Germany: Bruker AXS.

Carter-Stiglitz, B., Moskowitz, B., Solheid, P., Berquó, T. S., Jackson, M., & Kosterov, A. (2006). Low-temperature magnetic behavior of multidomain titanomagnetites: TM0, TM16, and TM35. *Journal of Geophysical Research*, *111*, B12S05. https://doi.org/10.1029/2006JB004561

Charilaou, M., Kind, J., Koulialias, D., Weidler, P. G., Mensing, C., Löffler, J. F., & Gehring, A. U. (2015). Magneto-electronic coupling in modulated defect-structures of natural $Fe_{1-x}S$. *Journal of Applied Physics*, *118*(8), 083903. https://doi.org/10.1063/1.4929634

Cheary, R. W., & Coelho, A. A. (1992). A fundamental parameters approach to X-ray line-profile fitting. *Journal of Applied Crystallography*, *25*(2), 109–121. https://doi.org/10.1107/S0021889891010804

Church, N., Feinberg, J. M., & Harrison, R. (2011). Low-temperature domain wall pinning in titanomagnetite: Quantitative modeling of multidomain first-order reversal curve diagrams and AC susceptibility. *Geochemistry, Geophysics, Geosystems*, *12*, Q07Z27. https://doi.org/10.1029/2011GC003538

Clark, D. C., & Kelly, W. C. (1973). Sulfide deformation study: I. Experimental deformation of pyrrhotite and sphalerite to 2000 bars and 500°C. *Economic Geology*, *68*(3), 332–352. https://doi.org/10.2113/gsecongeo.68.3.332

Dekkers, M. J., Mattéi, J.-L., Fillion, G., & Rochette, P. (1989). Grain-size dependence of the magnetic behavior of pyrrhotite during its low-temperature transition at 34 K. *Geophysical Research Letters*, *16*(8), 855–858. https://doi.org/10.1029/GL016i008p00855

Dunlop, D., & Özdemir, Ö. (1997). *Rock Magnetism. Fundamentals and Frontiers*. Cambridge, UK: Cambridge University Press. https://doi.org/10.1017/CBO9780511612794

Engel, R. F., Peacor, D. R., & Kelly, W. C. (1978). A new 5C pyrrhotite. *American Mineralogist*, *63*, 1274–1277.

Fillion, G., Mattéi, J.-L., Rochette, P., & Wolfers, P. (1992). Neutron study of 4C pyrrhotite. *Journal of Magnetism and Magnetic Materials*, *104-107*, 1985–1986. https://doi.org/10.1016/0304-8853(92)91633-5

Fillion, G., & Rochette, P. (1988). The low-temperature transition in monoclinic pyrrhotite. *Journal de Physique, Colloques*, *C8*, 907–908.

Friedman, S. A., Feinberg, J. M., Ferré, E. C., Demory, F., Martín-Hernández, F., Conder, J. A., & Rochette, P. (2014). Craton vs. rift uppermost mantle contributions to magnetic anomalies in the United States interior. *Tectonophysics*, *624-625*, 15–23. https://doi.org/10.1016/j.tecto.2014.04.023

Gaunt, P. (1983). Ferromagnetic domain wall pinning by a random array of inhomogeneities. *Philosophical Magazine B*, *48*(3), 261–276. https://doi.org/10.1080/13642818308228288

Gillett, S. L. (2003). Paleomagnetism of the notch peak contact metamorphic aureole, revisited: Pyrrhotite from magnetite+pyrite under submetamorphic conditions. *Journal of Geophysical Research*, *108*(B9), 2446. https://doi.org/10.1029/2002JB002386

Goodenough, J. B. (1963). *Magnetism and the Chemical Bond*. New York: Wiley.

Graf, J. L., & Skinner, B. J. (1970). Strength and deformation of pyrite and pyrrhotite. *Economic Geology*, *65*(2), 206–215. https://doi.org/10.2113/gsecongeo.65.2.206

Grazulis, S., Chateigner, D., Downs, R. T., Yokochi, A. T., Quiros, M., Lutterotti, L., et al. (2009). Crystallography open database—An open-access collection of crystal structures. *Journal of Applied Crystallography*, *42*(4), 726–729. https://doi.org/10.1107/S0021889809016690

Hafner, S., & Kalvius, M. (1966). The Mössbauer resonance of Fe in troilite and pyrrhotite. *Zeitschrift für Kristallographie*, *123*(6), 443–458. https://doi.org/10.1524/zkri.1966.123.6.443

Halgedahl, S. L., & Fuller, M. (1981). The dependence of magnetic domain structure upon magnetization state in polycrystalline pyrrhotite. *Physics of the Earth and Planetary Interiors*, *26*(1-2), 93–97. https://doi.org/10.1016/0031-9201(81)90101-1

Harries, D., Pollok, K., & Langenhorst, F. (2011). Translation interface modulation in NC-pyrrhotites: Direct imaging by TEM and a model toward understanding partially disordered structural states. *American Mineralogist*, *96*(5-6), 716–731. https://doi.org/10.2138/am.2011.3644

Herbert, F. W., Krishnamoorthy, A., Yildiz, B., & Van Vliet, K. J. (2015). Diffusion-limited kinetics of the antiferromagnetic ferrimagnetic λ-transition in $Fe_{1-x}S$. *Applied Physics Letters*, *106*(9), 092402. https://doi.org/10.1063/1.4913201

Honsho, C., Yamazaki, T., Ura, T., Okino, K., Morozumi, H., & Ueda, S. (2016). Magnetic anomalies associated with abundant production of pyrrhotite in a sulfide deposit in the Okinawa trough, Japan. *Geochemistry, Geophysics, Geosystems*, *17*, 4413–4424. https://doi.org/10.1002/2016GC006480

Jackson, M., Worm, H.-U., & Banerjee, S. K. (1990). Fourier analysis of digital hysteresis data: Rock magnetic applications. *Physics of the Earth and Planetary Interiors*, *65*(1-2), 78–87. https://doi.org/10.1016/0031-9201(90)90077-B

Kars, M., Aubourg, C., & Suárez-Ruiz, I. (2015). Neoformed magnetic minerals as an indicator of moderate burial: The key example of middle Paleozoic sedimentary rocks, West Virginia. *AAPG Bulletin*, *99*(03), 389–401. https://doi.org/10.1306/06301413006

Kasama, T., Church, N. S., Feinberg, J. M., Dunin-Borkowski, R. E., & Harrison, R. J. (2010). Direct observation of ferrimagnetic/ferroelastic domain interactions in magnetite below the Verwey transition. *Earth and Planetary Science Letters*, *297*, 10–17.

Keller-Besrest, F., Collin, G., & Comes, R. (1982). Structure and planar faults in defective NiAs-type compound 3C Fe_7S_8. *Acta Crystallographica B38*, 296–303.

Kind, J., García-Rubio, I., Charilaou, M., Nowaczyk, N. R., Löffler, J. F., & Gehring, A. U. (2013). Domain-wall dynamics in 4C pyrrhotite at low temperature. *Geophysical Journal International*, *195*(1), 192–199. https://doi.org/10.1093/gji/ggt262

Kontny, A., de Wall, H., Sharp, T. G., & Pósfai, M. (2000). Mineralogy and magnetic behavior of pyrrhotite from a 260 °C section at the KTB drilling site, Germany. *American Mineralogist*, *85*(10), 1416–1427. https://doi.org/10.2138/am-2000-1010

Koulialias, D., Charilaou, M., Mensing, C., Löffler, J. F., & Gehring, A. U. (2018). Torque analysis of incoherent spin rotation in the presence of ordered defects. *Applied Physics Letters*, *112*(20), 202404. https://doi.org/10.1063/1.5023886

Koulialias, D., Charilaou, M., Schäublin, R., Mensing, C., Weidler, P. G., Löffler, J. F., & Gehring, A. U. (2018). Ordered defects in $Fe_{1-x}S$ generate additional magnetic anisotropy symmetries. *Journal of Applied Physics*, *123*(3), 033902. https://doi.org/10.1063/1.5007830

Koulialias, D., Kind, J., Charilaou, M., Weidler, P. G., Löffler, J. F., & Gehring, A. U. (2016). Variable defect structures cause the magnetic low-temperature transition in natural monoclinic pyrrhotite. *Geophysical Journal International*, *204*(2), 961–967. https://doi.org/10.1093/gji/ggv498

Kübler, L. (1985). Deformation mechanisms in experimentally deformed single crystals of Pyrrhotite, $Fe_{1-x}S$. *Physics and Chemistry of Minerals*, *12*(6), 353–362. https://doi.org/10.1007/BF00654346

Letard, I., Sainctavit, P., & Deudon, C. (2007). XMCD at Fe $L_{2,3}$ edges, Fe and S K edges on Fe_7S_8. *Physics and Chemistry of Minerals*, *34*(2), 113–120. https://doi.org/10.1007/s00269-006-0132-8

Li, F., & Franzen, H. F. (1996). Ordering, incommensuration, and phase transitions in pyrrhotite. Part II: A high-temperature X-ray powder diffraction and thermomagnetic study. *Journal of Solid State Chemistry*, *126*(1), 108–120. https://doi.org/10.1006/jssc.1996.0318

Lindquist, A. K., Feinberg, J. M., Harrison, R. J., Loudon, J. C., & Newell, A. J. (2015). Domain wall pinning and dislocations: Investigating magnetite deformed under conditions analogous to nature using transmission electron microscopy. *Journal of Geophysical Research: Solid Earth*, *120*, 1415–1430. https://doi.org/10.1002/2014JB011335

Louzada, K. L., Stewart, S. T., & Weiss, B. J. (2007). Effect of shock on the magnetic properties of pyrrhotite, the Martian crust, and meteorites. *Geophysical Research Letters*, *34*, L05204. https://doi.org/10.1029/2006GL027685

Lyubutin, I. S., Lin, C.-R., Lu, S.-Z., Siao, Y.-J., Korzhetskiy, Y. V., Dmitrieva, T. V., et al. (2011). High-temperature redistribution of cation vacancies and irreversible magnetic transitions in the $Fe_{1-x}S$ nanodisks observed by the Mössbauer spectroscopy and magnetic measurements. *Journal of Nanoparticle Research*, *13*(10), 5507–5517. https://doi.org/10.1007/s11051-011-0538-1

Mang, C., Kontny, A., Harries, D., Langenhorst, F., & Hecht, L. (2012). Iron deficiency in pyrrhotite of suevites from the Chesapeake Bay impact crater, USA—A consequence of shock metamorphism? *Meteoritics and Planetary Science*, *47*(2), 277–295. https://doi.org/10.1111/j.1945-5100.2012.01329.x

Manning, E. B., & Elmore, R. D. (2012). Rock magnetism and identification of remanence components in the Marcellus shale. In R. D. Elmore, et al. (Eds.), *Pennsylvania, Remagnetization and Chemical Alteration of Sedimentary Rocks*, *Geological Society London Special Publications* (Vol. 371, pp. 271–282).

Marusak, L. A., & Mulay, L. N. (1980). Polytypism in the cation-deficient iron sulfide Fe_9S_{10}, and the magnetokinetics of the diffusion process at temperatures about the antiferro- to ferrimagnetic (λ) phase transition. *Physical Review B*, *21*(1), 238–244. https://doi.org/10.1103/PhysRevB.21.238

Néel, L. (1953). Some new results on antiferromagnetism and ferromagnetism. *Reviews of Modern Physics*, *25*(1), 58–63. https://doi.org/10.1103/RevModPhys.25.58

Oddou, J. L., Jeandey, C., Mattéi, J.-L., & Fillion, G. (1992). Mössbauer study of the low-temperature transition in pyrrhotite. *Journal of Magnetism and Magnetic Materials*, *104-107*, 1987–1988. https://doi.org/10.1016/0304-8853(92)91634-6

O'Reilly, W. O., Hoffmann, V., Chouker, A. C., Soffel, H. C., & Menyeh, A. (2000). Magnetic properties of synthetic analogues of pyrrhotite ore in the grain size range 1–24 μm. *Geophysical Journal International*, *142*(3), 669–683. https://doi.org/10.1046/j.1365-246x.2000.00169.x

Özdemir, Ö. (2000). Coercive force of single crystals of magnetite at low temperatures. *Geophysical Journal International*, *141*(2), 351–356. https://doi.org/10.1046/j.1365-246x.2000.00081.x

Pauthenet, R. (1952). Étude magnétique d'un monocristal de pyrrhotine aux basses températures. *Comptes Rendus de l'Académie des Sciences*, *234*, 2261.

Pearce, C. I., Pattrick, A. D., & Vaughan, D. J. (2006). Electrical and magnetic properties of sulfides. *Reviews in Mineralogy and Geochemistry*, *61*(1), 127–180. https://doi.org/10.2138/rmg.2006.61.3

Pierce, L., & Buseck, P. R. (1974). Electron imaging of pyrrhotite superstructures. *Science*, *186*, 2209–2212.

Pósfai, M., Sharp, T. G., & Kontny, A. (2000). Pyrrhotite varieties from the 9.1 km deep borehole of the KTB project. *American Mineralogist*, *85*(10), 1406–1415. https://doi.org/10.2138/am-2000-1009

Powell, A. V., Vaqueiro, P., Knight, K. S., Chapon, L. C., & Sánchez, R. D. (2004). Structure and magnetism in synthetic pyrrhotite Fe_7S_8: A powder neutron-diffraction study. *Physical Review B*, *70*(1), 014415. https://doi.org/10.1103/PhysRevB.70.014415

Rochette, P., Fillion, G., & Dekkers, M. J. (2011). The low-temperature magnetic transition of monoclinic pyrrhotite. *The IRM Quarterly*, *21*(1), 1.

Rochette, P., Fillion, G., Mattéi, J.-L., & Dekkers, M. J. (1990). Magnetic transition at 30-34 Kelvin in pyrrhotite: Insight into a widespread occurrence of this mineral in rocks. *Earth and Planetary Science Letters*, *98*, 319–328.

Rochette, P., Lorand, J.-P., Fillion, G., & Sautter, V. (2001). Pyrrhotite and remanent magnetization of SNC meteorites: A changing perspective on Martian magnetism. *Earth and Planetary Science Letters*, *190*, 1–12.

Sakkopoulos, S., Vitoratos, E., & Argyreas, T. (1986). Correlation between chemical bonds and properties in pyrrhotite. *Journal of Chemical Education*, *63*(8), 665–666. https://doi.org/10.1021/ed063p665

Schill, E., Appel, E., Godin, L., Crouzet, C., Gautam, P., & Regmi, K. R. (2003). Record of deformation by secondary magnetic remanences and magnetic anisotropy in the Nar/Phu valley (central Himalaya). *Tectonophysics*, *377*(1-2), 197–209. https://doi.org/10.1016/j.tecto.2003.08.020

Schwarz, E. J., & Vaughan, D. J. (1972). Magnetic phase relations of pyrrhotite. *Journal of Geomagnetism and Geoelectricity*, *24*(4), 441–458. https://doi.org/10.5636/jgg.24.441

Stadelmann, P. A. (1987). EMS—A software package for electron-diffraction analysis and HREM image simulation in materials science. *Ultramicroscopy*, *21*(2), 131–145. https://doi.org/10.1016/0304-3991(87)90080-5

Tokonami, M., Nishiguchi, K., & Morimoto, N. (1972). Crystal structure of a monoclinic pyrrhotite (Fe_7S_8). *American Mineralogist*, *57*, 1066–1080.

Van Landuyt, J., & Amelinckx, S. (1972). Electron microscope observations of the defect structure of pyrrhotite. *Materials Research Bulletin*, *7*(1), 71–79. https://doi.org/10.1016/0025-5408(72)90071-2

Volk, M. W. R., Gilder, S. A., & Feinberg, J. M. (2016). Low temperature magnetic properties of monoclinic pyrrhotite with particular relevance to the Besnus transition. *Geophysical Journal International*, *207*(3), 1783–1795. https://doi.org/10.1093/gji/ggw376

Weaver, R., Roberts, A. P., & Barker, A. J. (2002). A late diagenetic, (syn-folding) magnetization carried by pyrrhotite: Implications for paleomagnetic studies from magnetic iron sulphide-bearing sediments. *Earth and Planetary Science Letters*, *200*(3-4), 371–386. https://doi.org/10.1016/S0012-821X(02)00652-0

Weiss, P. (1899). Sur l'aimantation plane de la pyrrhotine. *Journal of Theorological and Applied Physics*, *8*(1), 542–544. https://doi.org/10.1051/jphystap:018990080054200

Weiss, P. (1907). L'hypothèse du champ moléculaire et la propriété ferromagnétique. *Journal of Theorological and Applied Physics*, *6*(1), 661–690. https://doi.org/10.1051/jphystap:019070060066100

Winklhofer, M., & Zimanyi, T. (2006). Extracting the intrinsic switching field distribution in perpendicular media: A comparative analysis. *Journal of Applied Physics*, *99*, 08E710.

Wolfers, P., Fillion, G., Ouladdiaf, B., Ballou, R., & Rochette, P. (2011). The pyrrhotite 32 K magnetic transition. *Solid State Phenomena*, *170*, 174–179. https://doi.org/10.4028/www.scientific.net/SSP.170.174

Wright, J. B. (1966). Studies on the pyrrhotite and paragenesis of the Moke creek sulphide lode, Wakatipu district. *New Zealand Journal of Geology and Geophysics*, *9*(3), 301–322.